





Article

Synthesis, Bottom up Assembly and Thermoelectric Properties of Sb-Doped PbS Nanocrystal Building Blocks

Doris Cadavid ^{1,*}, Kaya Wei ², Yu Liu ^{3,4}, Yu Zhang ³, Mengyao Li ³, Aziz Genç ⁵, Taisiia Berestok ³, Maria Ibáñez ⁴, Alexey Shavel ³, George S. Nolas ^{2,*} and Andreu Cabot ^{3,6,*}

- ¹ Departamento de Física, Universidad Nacional de Colombia, Ciudad Universitaria, Bogotá 111321, Colombia
² Department of Physics, University of South Florida, Tampa, FL 33620, USA; kayawei@mail.usf.edu
³ Catalonia Institute for Energy Research-IREC, Sant Adrià de Besòs, 08930 Barcelona, Spain; liuyu92525@gmail.com (Y.L.); tingchan99@gmail.com (Y.Z.); limengyaorz@gmail.com (M.L.); taisiia.berestok@gmail.com (T.B.); al.shavel@gmail.com (A.S.)
⁴ Am Campus 1, Institute of Science and Technology Austria, 3400 Klosterneuburg, Austria; mibanez@ist.ac.at
⁵ Department of Materials Science and Engineering, Faculty of Engineering, Izmir Institute of Technology, Urla, İzmir 35430, Turkey; azizgenc@gmail.com
⁶ ICREA (Institució Catalana de Recerca i Estudis Avançats), Pg. Lluís Companys 23, 08010 Barcelona, Spain
* Correspondence: dycadavidr@unal.edu.co (D.C.); gnolas@usf.edu (G.S.N.); acabot@irec.cat (A.C.)

Abstract: The precise engineering of thermoelectric materials using nanocrystals as their building blocks has proven to be an excellent strategy to increase energy conversion efficiency. Here we present a synthetic route to produce Sb-doped PbS colloidal nanoparticles. These nanoparticles are then consolidated into nanocrystalline PbS:Sb using spark plasma sintering. We demonstrate that the introduction of Sb significantly influences the size, geometry, crystal lattice and especially the carrier concentration of PbS. The increase of charge carrier concentration achieved with the introduction of Sb translates into an increase of the electrical and thermal conductivities and a decrease of the Seebeck coefficient. Overall, PbS:Sb nanomaterial were characterized by two-fold higher thermoelectric figures of merit than undoped PbS.

Keywords: nanocrystals; thermoelectrics; bottom-up engineering; doping; chalcogenides; lead sulfide



Citation: Cadavid, D.; Wei, K.; Liu, Y.; Zhang, Y.; Li, M.; Genç, A.; Berestok, T.; Ibáñez, M.; Shavel, A.; Nolas, G.S.; et al. Synthesis, Bottom up Assembly and Thermoelectric Properties of Sb-Doped PbS Nanocrystal Building Blocks. *Materials* **2021**, *14*, 853. <https://doi.org/10.3390/ma14040853>

Academic Editor: P. Davide Cozzoli
Received: 22 December 2020
Accepted: 5 February 2021
Published: 10 February 2021

Publisher's Note: MDPI stays neutral with regard to jurisdictional claims in published maps and institutional affiliations.



Copyright: © 2021 by the authors. Licensee MDPI, Basel, Switzerland. This article is an open access article distributed under the terms and conditions of the Creative Commons Attribution (CC BY) license (<https://creativecommons.org/licenses/by/4.0/>).

1. Introduction

To exploit the full potential of bottom-up strategies to produce functional nanomaterials, it is necessary to develop strategies to control the charge carrier concentration [1,2]. However, introducing controlled amounts of electronic dopants into colloidal nanocrystals (NCs) has been often a main challenge. A particular application, where such electronic doping is key and where the use of nanomaterials presents a clear advantage, is thermoelectricity [3–6]. All relevant thermoelectric properties, electrical conductivity (σ), Seebeck coefficient (S) and thermal conductivity (κ), strongly depend on charge carrier concentration. While σ increases with charge carrier concentration, thus improving the thermoelectric figure of merit $ZT = \sigma S^2 / \kappa$, S decreases and the electronic contribution to κ increases, both having a detrimental effect on ZT [7,8]. Thus, a precise adjustment of the carrier concentration is necessary to optimize the material's thermoelectric properties.

The research on thermoelectric materials typically aims to identify good candidate materials and optimize their properties to maximize ZT . Since the ZT of a material peaks at an optimum carrier concentration, once identified a potential candidate, the strategy to follow is to optimize its charge carrier concentration. At the same time, one needs to decouple as much as possible the three transport parameters, σ , S and κ , to maximize the thermoelectric efficiency [9,10].

Nanostructuring has resulted in high-performance thermoelectric materials, characterized by reduced κ due to phonon scattering at grain boundaries [3,11–14]. Nanomaterials may also display enhanced S when correctly designed and precisely engineered. In this

scenario, processing of thermoelectric nanomaterials by bottom-up assembly of colloidal NCs is particularly interesting [5,14–21]. Colloidal NCs with controlled size, shape, crystallographic phase and composition are ideal building blocks to produce nanostructured materials with well-tuned parameters [15,16,22–28]. From a fundamental point of view, these well-controlled systems can be used to gain further understanding of the mechanisms and processes underlying the thermoelectric effect. From an application point of view, such well-controlled systems produced by solution-processing technologies may hold the key to cost-effective thermoelectric devices in a wide range of applications [29].

To produce optimally doped NCs, it is crucial to control their surface chemistry. There is a large number of atoms at the NC surface, which may have dangling bonds that act as traps or electron donors. These dangling bonds may be passivated by organic or inorganic ligands that can be introduced during the synthesis or by ligand exchange, but that may also be adsorbed from the environment, as in the case of oxygen or hydroxyl molecules [30–33].

Due to its relative simplicity and high performance, one particularly interesting thermoelectric material is PbS. N-type PbS, doped with PbCl₂ and mixed with a small fraction of a second nano-precipitated phase such as PbTe [34], PbSe [35], Sb₂S₃ or Bi₂S₃ [36] has reached *ZT* values up to 0.8 at 770 K, 1.3 at 900 K, 0.79 at 723 K and 1.1 at 923 K, respectively. P-type PbS doped with Na and mixed with SrS [37] or CdS [38] secondary phases has reached *ZT* values of up to 1.2 and 1.3 at 923 K, respectively. Regarding the bottom-up approach, Cl-doped PbTe_xSe_{1-x}@PbS core-shell NCs reached thermoelectric figures of merit of up to 0.94 at 700 K [32], and PbS-Ag nanocomposites produced by strategic engineering of nano-scale building blocks and interfaces using PbS NCs resulted in thermoelectric figures of merit of up to 1.7 at 850 K [13]. In general, this last strategy proved successful in introducing metals, such as Cu or Sn, into the materials with reported figures of merit of 0.86 and 0.88 at 855 K [39]. Besides, in the lead chalcogenide family, PbTe with a co-doping of silver and antimony or bismuth, also present higher thermoelectric efficiency due to the inhomogeneities resulting from Ag or Sb segregation [40,41].

In this work, we demonstrate that Sb-doping in colloidal PbS NCs can be employed to tune the carrier concentration of bottom-up processed nanocrystalline materials. We detail here the synthesis protocol to produce the Sb-doped PbS NCs and the results from characterizing the nanomaterial resulting from the spark plasma sintering (SPS) of the NCs at 400 °C. We chose Sb as n-type donor since Sb³⁺ substitutes Pb²⁺ in the case of PbTe [42] resulting in n-type doping [43].

2. Materials and Methods

2.1. Materials

Lead (II) oxide (PbO, 99.9%), elemental sulfur (99.998%), antimony (III) acetate (99.99%), oleic acid (OAc, tech. 90%), 1-octadecene (ODE, 90%), oleylamine (OAm, tech. 70%), sodium sulfide nonahydrate (NaS·9H₂O 99.99%), and ethylene glycol (EG, 99.5%) were purchased from Aldrich (St. Louis, MO, USA). Chloroform, hexane, and ethanol were of analytical grade and obtained from various sources. All chemicals were used as received, without further purification. All syntheses were carried out using a vacuum/dry argon gas Schlenk line and argon glovebox for storing and handling air- and moisture-sensitive chemicals.

2.2. Synthesis of PbS Nanocrystals

PbS NCs were prepared following a reported procedure [32]. In a typical synthesis, 4.46 g of lead oxide (20 mmol) and 50 mL of OAc (0.159 mol) were mixed with 100 mL of ODE (0.312 mol). This mixture was heated to 130 °C and maintained at this temperature for 1 h under vacuum to form the lead oleate complex. This precursor solution was then flushed with Ar and heated to 210 °C. At this temperature, a sulfur precursor, prepared by dissolving 0.64 g of elemental sulfur (20 mmol) in 20 mL of distilled OAm (0.061 mol), was rapidly injected. Sb-doped PbS NCs were obtained by introducing different quantities (from 2 mmol, 3 mmol and 5 mmol) of Sb (III) acetate in the precursor solution. The

reaction mixture was maintained between 195 °C and 210 °C for 5 min and then quickly cooled down to room temperature using a water bath. PbS NCs were washed by multiple precipitation/re-dispersion steps using ethanol as a non-solvent and hexane as solvent.

2.3. Removal of the Capping Ligands

In a typical procedure, a stock 0.1 M solution of Na₂S·9H₂O in EG was prepared, and as-synthesized PbS NCs (300 mg) were dispersed in 10 mL of chloroform. Ligand exchange was performed by adding 5 mL of a Na₂S·9H₂O solution to the NCs in CHCl₃. After stirring for 30 min under Ar, the solution was precipitated at 3000 rpm. During the stirring, NCs were displaced from chloroform to EG solution. NCs were then thoroughly purified using chloroform to remove the remaining organic species. Finally, the PbS NCs were precipitated, dried and stored in a glove box until posterior use.

2.4. Structural and Chemical Characterization of PbS and Sb-Doped PbS NCs

X-ray power diffraction (XRD) analyses were carried out on an AXS D8 Advance X-ray diffractometer (Bruker, Rosenheim, Germany) with Cu K α 1 radiation ($\lambda = 1.5406 \text{ \AA}$). The size and shape of the nanoparticles were examined by transmission electron microscopy (TEM) (TEM Libra 120, Zeiss, Oberkochen, Germany) using a Libra 120 (Zeiss, Oberkochen, Germany) operating at 120 keV accelerating voltage and high resolution TEM (HRTEM), high-angle annular dark-field imaging (HAADF-STEM) (Jeol, Tokyo, Japan) and electron energy-loss spectroscopy (EELS) (Zeiss, Oberkochen, Germany) in a Jeol 2010F (Jeol, Tokyo, Japan) field emission gun microscope operated at 200 kV. Scanning electron microscopy (SEM) (Jeol, Tokyo, Japan) was performed using a Zeiss Auriga microscope (Zeiss, Oberkochen, Germany) with an energy dispersive X-ray spectroscopy (EDX) detector to study the material's composition.

2.5. Consolidation and Thermoelectric Characterization of PbS and Sb-Doped PbS NCs

Nanoparticles were consolidated into dense nanomaterials using spark plasma sintering (SPS) in a commercial instrument (Version: 10–3, Thermal Technology LLC Inc, Santa Rosa, CA, USA). The sintering of PbS and Sb-doped PbS NCs were carried out at 60 MPa and 400 °C for 10 min, resulting in pellets with densities of 90% and 94% of the theoretical value, respectively. The thermoelectric properties of the nanocrystalline materials were characterized by using a custom design radiation-shielded vacuum probe. Temperature dependent four-probe resistivity ($\rho = 1/\sigma$, S (gradient sweep method), and steady-state κ were measurements from 12 to 300 K with uncertainties of 4, 6, and 8%, respectively [44,45]. The samples were cut by a wire saw into parallelepipeds of $2 \times 2 \times 5 \text{ mm}^3$ in order to conduct these measurements. The Hall measurements were conducted in a four-probe configuration (on $0.5 \times 2 \times 5 \text{ mm}^3$ samples cut by a wire saw) using an electromagnet that generated a magnetic field up to 1.2 T. Current was passed through the specimen while the field was varied between 0.1 T and 1 T in increments of 0.1 T with an inversion of the field to eliminated voltage probe misalignment effects.

3. Results and Discussion

Figure 1a shows a representative TEM micrograph of the PbS NCs obtained by the reaction of lead oleate with sulfur in the presence of OAm and OAc, following the above-detailed procedure. PbS NCs were highly monodisperse and displayed a cubic morphology. Their size could be controlled in the range from 8 nm to 12 nm by changing the reaction temperature from 130 °C to 210 °C. Their crystal structure was identified as cubic galena (Fm-3m, JCPDS 5-0592) by means of HRTEM (Figure 1a inset) and XRD (Figure 1c). The introduction of Sb ions in the precursor solution clearly influenced the particle morphology. The presence of Sb resulted in irregular shaped Pb_{1-x}Sb_xS NCs having broader size distributions (Figure 1b). The PbS crystallographic phase remained unchanged as observed from HRTEM (Figure 2a) and XRD analyses (Figure 1c). However, the cubic crystal lattice was noticeably modified by the presence of Sb. It was observed that Sb incorporation affected

the relative XRD peak intensity and the lattice parameter (Figure 1c inset). Observed differences are related to both the loss of the cubic morphology of the NCs, and to a strain within the formed $\text{Pb}_{1-x}\text{Sb}_x\text{S}$ NCs. No secondary phases were identified in our XRD data even with the specimen prepared at the highest concentration of Sb precursor.

EELS analysis of several $\text{Pb}_{1-x}\text{Sb}_x\text{S}$ NCs did not show a significant change in Sb composition from particle to particle. However, EELS analysis also showed that Sb was not homogeneously distributed within each $\text{Pb}_{1-x}\text{Sb}_x\text{S}$ NC but a radial gradient of Sb was observed, with the Sb concentration higher in the outermost layers of the NC than in the center (Figure 1b inset). In terms of composition, ICP and EDX analysis (Figure 2b), showed the Sb content of the NCs $\text{Pb}_{1-x}\text{Sb}_x\text{S}$ (with $x = 0.15$ nominal) to be close to $x = 0.10$.

PbS and $\text{Pb}_{1-x}\text{Sb}_x\text{S}$ NCs were used as building blocks to produce PbS and $\text{Pb}_{1-x}\text{Sb}_x\text{S}$ polycrystalline materials with nano-scale grains. Before NCs consolidation into polycrystalline bulk materials, with the NCs still in solution, the surface ligands used to control the colloidal NCs solubility and growth during the synthesis were displaced using sodium sulfide. This step is considered to be fundamental to achieve high thermoelectric performances. As has been extensively demonstrated in previous works, the exchange of surface ligands in the surface of colloidal NCs affects the carrier mobility of the consolidated nanomaterials [25,46,47]. The removal of OAm/OAc by a $\text{Na}_2\text{S}\cdot 9\text{H}_2\text{O}$ solution improves the NCs interaction and reduces the amount of carbon in the final nanomaterial, which results in an increase of the charge carrier mobility. At the same time, it is well known, that ligands modify the NC surface chemistry [48]. In the particular case of OAc ligands, the annealing of NC-OAc samples usually results in an extensive surface oxidation that can be prevented by the displacement of OAc before sintering.

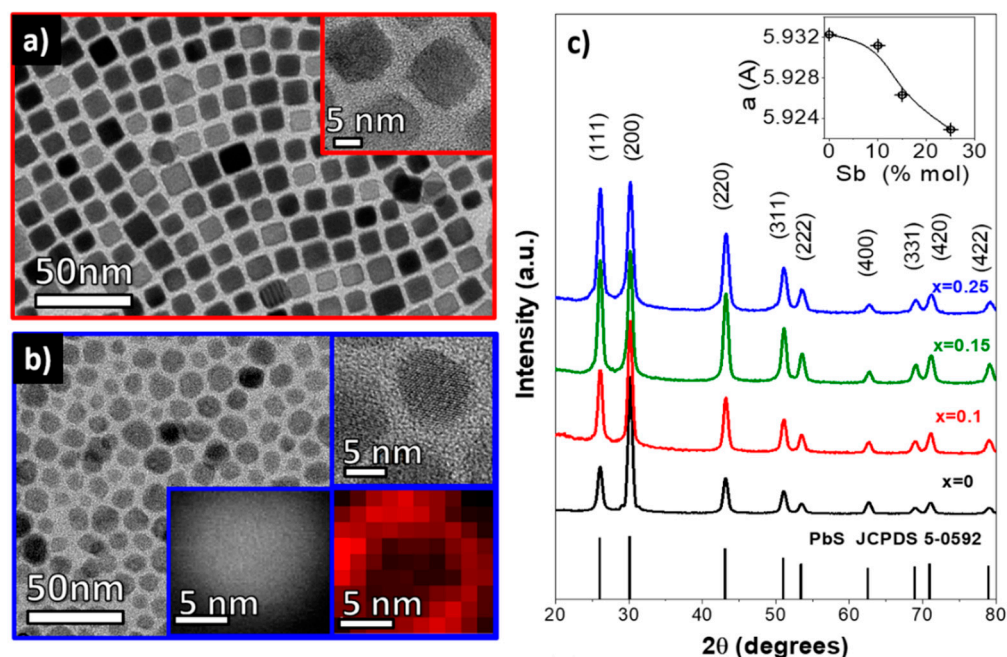


Figure 1. TEM and HRTEM (insets) micrographs of $\text{Pb}_{1-x}\text{Sb}_x\text{S}$ for $x = 0$ (a) and $x = 0.15$ (b) NCs. A HAADF-STEM image and an EELS elemental map with the distribution of Sb within a single PbS nanoparticle are also shown as insets of (b). The EELS map is taken by extracting the signal from the $M_{4,5}$ edge of Sb which starts at 528 eV. (c) XRD patterns of the $\text{Pb}_{1-x}\text{Sb}_x\text{S}$ NCs obtained with different nominal dopant concentrations of $x = 0, 0.1, 0.15$ and 0.25 .

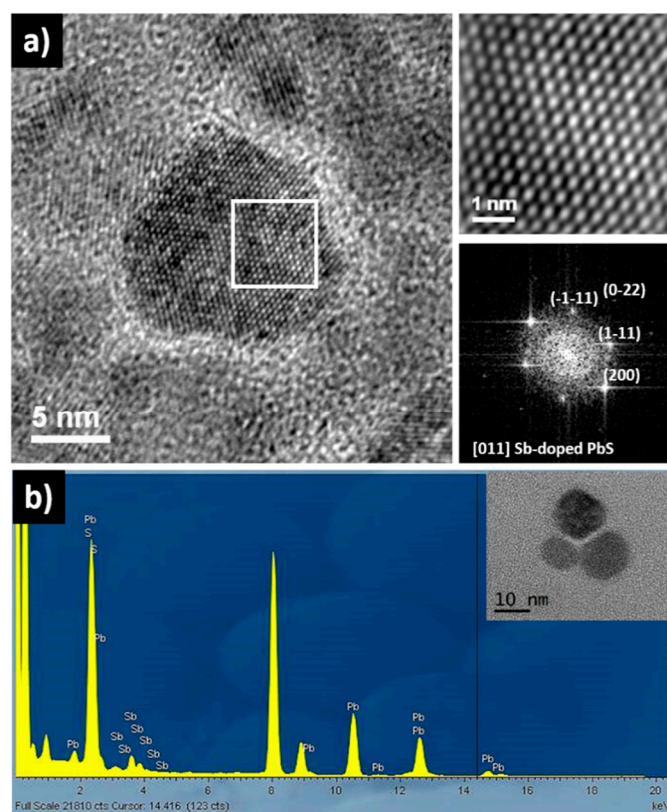


Figure 2. (a) HRTEM micrographs of $\text{Pb}_{1-x}\text{Sb}_x\text{S}$ NCs for $x = 0.15$, the crystal structure could be indexed as the galena PbS with face-centered cubic (fcc) symmetry belonging to $\text{Fm}\bar{3}\text{m}$ space group. The $\text{Pb}_{1-x}\text{Sb}_x\text{S}$ was zone axis $[011]$. (b) EDS spectrum of the same $\text{Pb}_{1-x}\text{Sb}_x\text{S}$ NCs showing the presence of Sb. EDS quantified the Sb composition at $x = 0.10$. Inset shows a TEM image of the NCs.

The final NCs were purified from residual organic molecules using chloroform and dried. The resulting nanopowders were consolidated into 12 mm diameter and 2 mm thick disk-shaped pellets using SPS at 400 °C and 60 MPa. The obtained pellets had densities between 90% and 94%. Figure 3 shows SEM micrographs of the consolidated PbS and $\text{Pb}_{1-x}\text{Sb}_x\text{S}$ polycrystalline materials. The crystal size domains increased by a factor of 10 during the SPS process.

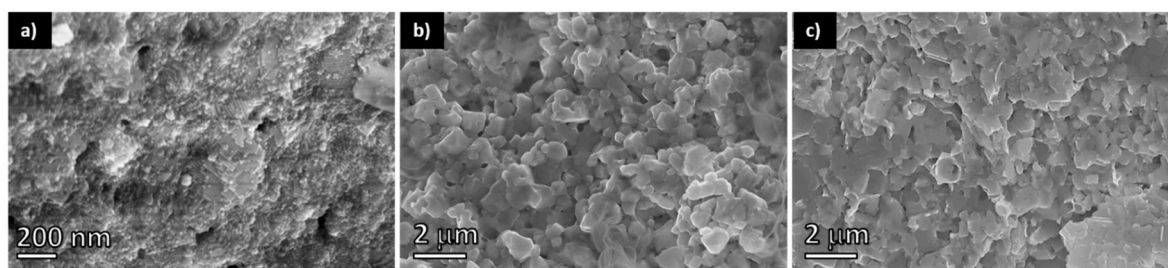


Figure 3. SEM micrographs of: (a) PbS nanopowder after ligand exchange; (b) PbS consolidated pellet; and (c) $\text{Pb}_{0.9}\text{Sb}_{0.1}\text{S}$ consolidated pellet.

Figure 4 shows the temperature dependence of σ , S , κ and ZT of PbS and $\text{Pb}_{0.9}\text{Sb}_{0.1}\text{S}$ polycrystalline materials. As expected, σ notably increased with Sb doping. Overall, almost a one order-of-magnitude increase in σ was observed with doping. On the other hand, a slight relative decrease of S and a moderate increase of κ , by a 20% and a 30% at 300 K, respectively, were also obtained. S decreases monotonically with the temperature and is negative for both materials. Its absolute value decrease with the Sb doping, due to

the increase of the charge carrier concentration. Regarding κ , it is important to analyze the behavior of its two contributions, the phononic or lattice thermal conductivity, κ_L , and the electronic thermal conductivity, κ_e . According to the Wiedermann–Franz law, κ_e increases due to the increase of σ for the Sb doped sample, as compared to the undoped sample. Additionally, the curves of κ present a peak around 50 K. This is because heat conduction in lightly/moderately doped semiconductor crystals is dominated by the lattice thermal conductivity contribution κ_L . At low temperatures ($T < \theta_D$) the mean free phonon path becomes large and the phonon movement is governed by point defects or boundary scattering, where $\kappa \sim T^{-1}$, whereas, at high temperatures the phonon scattering comes from umklapp processes that lead to a reduction in the mean free phonon path, and $\kappa \sim T^3$. Therefore, the peak observed in the trend of κ vs. T curve, Figure 4c, indicates the change in the scattering process between point defect/boundary scattering and umklapp scattering [8,49–51].

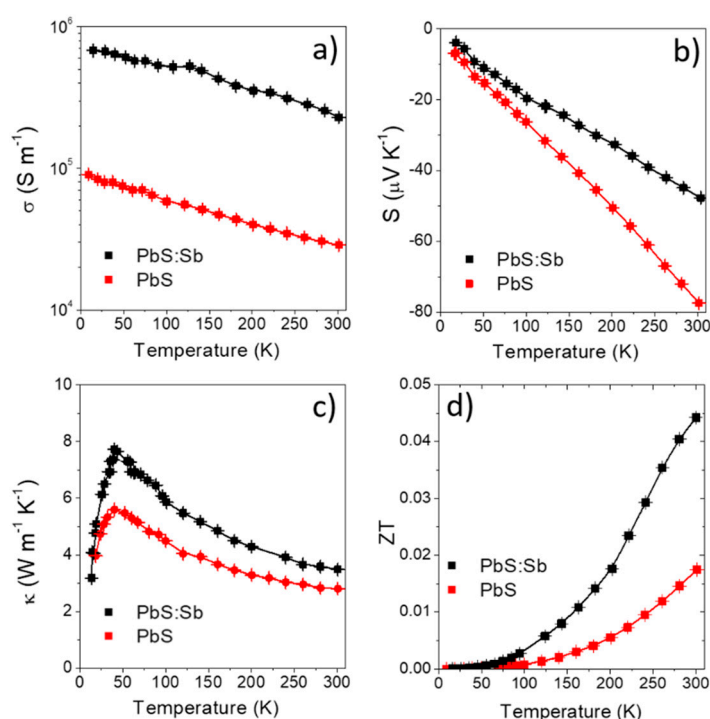


Figure 4. (a) Electrical conductivity, (b) Seebeck coefficient, (c) thermal conductivity and (d) thermoelectric figure of merit of PbS (red) and Pb_{0.9}Sb_{0.1}S (black) nanomaterials.

The large increase of σ obtained in the doped sample compensated for the decrease of S and the increase of κ , resulting in higher power factors ($PF = \sigma S^2$) and a two-fold increase in ZT . Hall measurements indicated that electrons are the majority carriers for both materials, with room temperature carrier concentrations of $6 \times 10^{19} \text{ cm}^{-3}$ and $9 \times 10^{19} \text{ cm}^{-3}$ for PbS and Pb_{0.9}Sb_{0.1}S, respectively (Table 1). As observed in PbTe:Sb, we assume Sb³⁺ substitutes Pb²⁺ ions providing one extra electron to the PbS conduction band. This n-type doping effect is consistent with the negative value of the Seebeck coefficients and the measured Hall charge carrier concentrations. The carrier concentration of polycrystalline PbS was relatively high, presumably related to an off-stoichiometric composition, PbS was Pb-rich, originated during either the ligand exchange or the consolidation process. This off-stoichiometry is difficult to control, which makes difficult the required tuning of the charge carrier concentration. Our work clearly indicates that it is more feasible to adjust the carrier concentration of bulk polycrystalline materials by doping PbS NCs with Sb.

Table 1. Charge carrier concentration and mobility of PbS and Pb_{0.9}Sb_{0.1}S, according to hall measurements.

Sample	Properties	Charge Carrier Concentration cm ⁻³	Charge Carrier Mobility cm ² /V s
PbS		6 × 10 ¹⁹	30
Pb _{0.9} Sb _{0.1} S		9 × 10 ¹⁹	154

Finally, Table 2 shows the state-of-the-art values of *ZT* for lead chalcogenide compounds doped with different elements for reference.

Table 2. State of the art of *ZT* values for lead chalcogenides compounds doped or mixed with different elements.

System	σ (S m ⁻¹ × 10 ⁴)	<i>S</i> (μV K ⁻¹)	κ (W m ⁻¹ K ⁻¹)	<i>ZT</i> (300K)	Ref.
PbS + Sb	23	−48	3.48	0.045	This Work
PbS + 4.6% Ag	8	−50	1.62	0.037	[13]
PbTe _{0.1} Se _{0.4} S _{0.5} -Cl	1	−75	1.25	0.013	[32]
(PbSe) _{0.88} (PbS) _{0.12} + 0.3% PbCl ₂	30	−75	2.9	0.17	[35]
Pb _{0.98} Na _{0.02} S	12.6	82	2.3	0.11	[37]
Pb _{0.975} Na _{0.025} S + 3.0% SrS	7.5	80	1.6	0.09	[38]
PbS + 4.9% Sn	3.8	−75	1.8	0.035	[39]

4. Conclusions

Sb-doped PbS NCs were produced by a novel colloidal synthesis protocol, with Sb radially distributed within the PbS NCs. Sb significantly modified the size, geometry and crystal lattice of PbS NCs. Bulk polycrystalline PbS with nano-scale grains were obtained from the assembly and SPS consolidation of the NCs. Doping of the PbS NCs with Sb allowed for a further increase in the carrier concentration of the consolidated polycrystalline material, resulting in a higher σ and a two-fold increase in *ZT* as compared with un-doped PbS.

Author Contributions: Conceptualization, D.C., G.S.N. and A.C.; methodology, D.C. and K.W.; formal analysis, D.C., K.W., M.I. and A.S.; investigation, D.C., K.W., Y.Z., Y.L., M.L.; A.G., T.B.; resources, A.C. and G.S.N.; writing—original draft preparation, D.C.; writing—review and editing, D.C., A.C. and G.S.N.; funding acquisition, A.C. and G.S.N. All authors have read and agreed to the published version of the manuscript.

Funding: This work was supported by European Regional Development Funds and the Framework 7 program under project UNION (FP7-NMP 310250). GSN acknowledges support from the US National Science Foundation under grant No. DMR-1748188. DC acknowledges support from COLCIENCIAS under project 120480863414.

Institutional Review Board Statement: Not applicable.

Informed Consent Statement: Not applicable.

Data Availability Statement: The data presented in this study are available within the article.

Conflicts of Interest: The authors declare no conflict of interest.

References

- Norris, D.J.; Efros, A.L.; Erwin, S.C. Doped nanocrystals. *Science* **2008**, *319*, 1776–1779. [[CrossRef](#)] [[PubMed](#)]
- Stavrinadis, A.; Konstantatos, G. Strategies for the controlled electronic doping of colloidal quantum dot solids. *ChemPhysChem* **2016**, *17*, 632–644. [[CrossRef](#)] [[PubMed](#)]

3. Liu, Y.; Zhang, Y.; Lim, K.H.; Ibáñez, M.; Ortega, S.; Li, M.; David, J.; Martí-Sánchez, S.; Ng, K.M.; Arbiol, J.; et al. High thermoelectric performance in crystallographically textured n-Type $\text{Bi}_2\text{Te}_{3-x}\text{Se}_x$ produced from asymmetric colloidal nanocrystals. *ACS Nano* **2018**, *12*, 7174–7184. [[CrossRef](#)]
4. Liu, Y.; García, G.; Ortega, S.; Cadavid, D.; Palacios, P.; Lu, J.; Ibáñez, M.; Xi, L.; De Roo, J.; López, A.M.; et al. Solution-based synthesis and processing of Sn- and Bi-doped Cu_3SbSe_4 nanocrystals, nanomaterials and ring-shaped thermoelectric generators. *J. Mater. Chem. A* **2016**, *5*, 2592–2602. [[CrossRef](#)]
5. Ibáñez, M.; Zamani, R.; Gorsse, S.; Fan, J.; Ortega, S.; Cadavid, D.; Morante, J.R.; Arbiol, J.; Cabot, A. Core-shell nanoparticles as building blocks for the bottom-up production of functional nano-composites: PbTe–PbS thermoelectric properties. *ACS Nano* **2013**, *7*, 2573–2586. [[CrossRef](#)]
6. Vaure, L.; Liu, Y.; Cadavid, D.; Agnese, F.; Aldakov, D.; Pouget, S.; Cabot, A.; Reiss, P.; Chenevier, P. Doping and surface effects of CuFeS_2 nanocrystals used in thermoelectric nanocomposites. *ChemNanoMat* **2018**, *4*, 982–991. [[CrossRef](#)]
7. Zebarjadi, M.; Joshi, G.; Zhu, G.; Yu, B.; Minnich, A.; Lan, Y.; Wang, X.; Dresselhaus, M.; Ren, Z.; Chen, G. Power factor enhancement by modulation doping in bulk nanocomposites. *Nano Lett.* **2011**, *11*, 2225–2230. [[CrossRef](#)]
8. Nolas, G.S.; Sharp, J.; Goldsmid, J. *Thermoelectrics: Basic Principles and New Materials Developments*; Springer Series in Materials Science; Springer: Berlin/Heidelberg, Germany, 2001; ISBN 978-3-540-41245-8.
9. Zevalkink, A.; Smiadak, D.M.; Blackburn, J.L.; Ferguson, A.J.; Chabynec, M.L.; Delaire, O.; Wang, J.; Kovnir, K.; Martin, J.; Schelhas, L.T.; et al. A practical field guide to thermoelectrics: Fundamentals, synthesis, and characterization. *Appl. Phys. Rev.* **2018**, *5*, 021303. [[CrossRef](#)]
10. Snyder, G.J.; Toberer, E.S. Complex thermoelectric materials. *Nat. Mater.* **2008**, *7*, 105–114. [[CrossRef](#)]
11. Ortega, S.; Ibáñez, M.; Liu, Y.; Zhang, Y.; Kovalenko, M.V.; Cadavid, D.; Cabot, A. Bottom-up engineering of thermoelectric nanomaterials and devices from solution-processed nanoparticle building blocks. *Chem. Soc. Rev.* **2017**, *46*, 3510–3528. [[CrossRef](#)] [[PubMed](#)]
12. Biswas, K.; He, J.; Blum, I.D.; Wu, C.-I.; Hogan, T.P.; Seidman, D.N.; Draid, V.P.; Kanatzidis, M.G. High-performance bulk thermoelectrics with all-scale hierarchical architectures. *Nature* **2012**, *489*, 414–418. [[CrossRef](#)] [[PubMed](#)]
13. Ibáñez, M.; Luo, Z.; Genç, A.; Piveteau, L.; Ortega, S.; Cadavid, D.; Dobrozhan, O.; Liu, Y.; Nachttegaal, M.; Zebarjadi, M.; et al. High-performance thermoelectric nanocomposites from nano-crystal building blocks. *Nat. Commun.* **2016**, *7*, 10766. [[CrossRef](#)] [[PubMed](#)]
14. Liu, Y.; Zhang, Y.; Ortega, S.; Ibáñez, M.; Lim, K.H.; Grau-Carbonell, A.; Martí-Sánchez, S.; Ng, K.M.; Arbiol, J.; Kovalenko, M.V.; et al. Crystallographically textured nanomaterials produced from the liquid phase sintering of $\text{Bi}_x\text{Sb}_{2-x}\text{Te}_3$ nanocrystal building blocks. *Nano Lett.* **2018**, *18*, 2557–2563. [[CrossRef](#)] [[PubMed](#)]
15. Cadavid, D.; Ibáñez, M.; Gorsse, S.; López, A.M.; Solano, E.; Morante, J.R.; Cabot, A. Bottom-up processing of thermoelectric nanocomposites from colloidal nanocrystal building blocks: The case of Ag_2Te – PbTe . *J. Nanopart. Res.* **2012**, *14*, 1328. [[CrossRef](#)]
16. Cadavid, D.; Ibáñez, M.; Shavel, A.; Durá, O.J.; de la Torre, M.A.L.; Cabot, A. Organic ligand displacement by metal salts to enhance nanoparticle functionality: Thermoelectric properties of Ag_2Te . *J. Mater. Chem. A* **2013**, *1*, 4864–4870. [[CrossRef](#)]
17. Datta, A.; Nolas, G.S. Synthesis and characterization of nanocrystalline FeSb_2 for thermoelectric applications. *Eur. J. Inorg. Chem.* **2011**, *2012*, 55–58. [[CrossRef](#)]
18. Wei, K.; Nolas, G.S. Synthesis and characterization of nanostructured stannite $\text{Cu}_2\text{ZnSnSe}_4$ and $\text{Ag}_2\text{ZnSnSe}_4$ for thermoelectric applications. *ACS Appl. Mater. Interfaces* **2015**, *7*, 9752–9757. [[CrossRef](#)] [[PubMed](#)]
19. Ibáñez, M.; Zamani, R.R.; Li, W.; Cadavid, D.; Gorsse, S.; Katcho, N.A.; Shavel, A.; López, A.M.; Morante, J.R.; Arbiol, J.; et al. Crystallographic control at the nanoscale to enhance functionality: Polytypic Cu_2GeSe_3 nanoparticles as thermoelectric materials. *Chem. Mater.* **2012**, *24*, 4615–4622. [[CrossRef](#)]
20. Ge, Z.-H.; Wei, K.; Lewis, H.; Martin, J.; Nolas, G.S. Bottom-up processing and low temperature transport properties of polycrystalline SnSe . *J. Solid State Chem.* **2015**, *225*, 354–358. [[CrossRef](#)]
21. Datta, A.; Nolas, G.S. Nanostructuring and porosity in anisotropic thermoelectric materials prepared by bottom-up processing. In *Thermoelectric Nanomaterials: Materials Design and Applications*; Springer Series in Materials Science; Koumoto, K., Mori, T., Eds.; Springer: Berlin/Heidelberg, Germany, 2013; pp. 177–191. ISBN 978-3-642-37537-8.
22. Ibáñez, M.; Cadavid, D.; Zamani, R.; García-Castelló, N.; Izquierdo-Roca, V.; Li, W.; Fairbrother, A.; Prades, J.D.; Shavel, A.; Arbiol, J.; et al. Composition control and thermoelectric properties of quaternary chalcogenide nanocrystals: The case of stannite $\text{Cu}_2\text{CdSnSe}_4$. *Chem. Mater.* **2012**, *24*, 562–570. [[CrossRef](#)]
23. Ibáñez, M.; Zamani, R.; LaLonde, A.; Cadavid, D.; Li, W.; Shavel, A.; Arbiol, J.; Morante, J.R.; Gorsse, S.; Snyder, G.J.; et al. $\text{Cu}_2\text{ZnGeSe}_4$ nanocrystals: Synthesis and thermoelectric properties. *J. Am. Chem. Soc.* **2012**, *134*, 4060–4063. [[CrossRef](#)]
24. Ortega, S.; Ibáñez, M.; Cadavid, D.; Cabot, A. Bottom-up processing of PbTe–PbS thermoelectric nanocomposites. *Int. J. Nanotechnol.* **2014**, *11*, 955–970. [[CrossRef](#)]
25. Cadavid, D.; Ortega, S.; Illera, S.; Liu, Y.; Ibáñez, M.; Shavel, A.; Zhang, Y.; Li, M.; López, A.M.; Noriega, G.; et al. Influence of the ligand stripping on the transport properties of nanoparticle-based PbSe nanomaterials. *ACS Appl. Energy Mater.* **2020**, *3*, 2120–2129. [[CrossRef](#)]
26. Martin, J.; Wang, L.; Chen, L.; Nolas, G.S. Enhanced Seebeck coefficient through energy-barrier scattering in PbTe nanocomposites. *Phys. Rev. B* **2009**, *79*, 115311. [[CrossRef](#)]

27. Martin, J.; Nolas, G.S.; Zhang, W.; Chen, L. PbTe nanocomposites synthesized from PbTe nanocrystals. *Appl. Phys. Lett.* **2007**, *90*, 222112. [[CrossRef](#)]
28. Wei, K.; Martin, J.; Nolas, G.S. Synthesis, SPS processing and low temperature transport properties of polycrystalline FeSb₂ with nano-scale grains. *Mater. Lett.* **2014**, *122*, 289–291. [[CrossRef](#)]
29. Kovalenko, M.V.; Manna, L.; Cabot, A.; Hens, Z.; Talapin, D.V.; Kagan, C.R.; Klimov, V.I.; Rogach, A.L.; Reiss, P.; Milliron, D.J.; et al. Prospects of nanoscience with nanocrystals. *ACS Nano* **2015**, *9*, 1012–1057. [[CrossRef](#)]
30. Capitani, C.; Pinchetti, V.; Gariano, G.; Santiago-González, B.; Santambrogio, C.; Campione, M.; Prato, M.; Brescia, R.; Camellini, A.; Bellato, F.; et al. Quantized electronic doping towards atomically controlled “charge-engineered” semiconductor nanocrystals. *Nano Lett.* **2019**, *19*, 1307–1317. [[CrossRef](#)]
31. Robin, A.; Livache, C.; Ithurria, S.; Lacaze, E.; Dubertret, M.N.B.; Lhuillier, E. Surface control of doping in self-doped nanocrystals. *ACS Appl. Mater. Interfaces* **2016**, *8*, 27122–27128. [[CrossRef](#)] [[PubMed](#)]
32. Ibáñez, M.; Korkosz, R.J.; Luo, Z.; Riba, P.; Cadavid, D.; Ortega, S.; Cabot, A.; Kanatzidis, M.G. Electron doping in bottom-up engineered thermoelectric nanomaterials through HCl-mediated ligand displacement. *J. Am. Chem. Soc.* **2015**, *137*, 4046–4049. [[CrossRef](#)]
33. Liu, Y.; Cadavid, D.; Ibáñez, M.; Roo, J.D.; Ortega, S.; Dobrozhan, O.; Kovalenko, M.V.; Cabot, A. Colloidal AgSbSe₂ nanocrystals: Surface analysis, electronic doping and processing into thermoelectric nanomaterials. *J. Mater. Chem. C* **2016**, *4*, 4756–4762. [[CrossRef](#)]
34. Johnsen, S.; He, J.; Androulakis, J.; Dravid, V.P.; Todorov, I.; Chung, D.Y.; Kanatzidis, M.G. Nanostructures boost the thermoelectric performance of PbS. *J. Am. Chem. Soc.* **2011**, *133*, 3460–3470. [[CrossRef](#)]
35. Androulakis, J.; Todorov, I.; He, J.; Chung, D.-Y.; Dravid, V.; Kanatzidis, M. Thermoelectrics from abundant chemical elements: High-performance nanostructured PbSe–PbS. *J. Am. Chem. Soc.* **2011**, *133*, 10920–10927. [[CrossRef](#)] [[PubMed](#)]
36. Zhao, L.-D.; Lo, S.-H.; He, J.; Li, H.; Biswas, K.; Androulakis, J.; Wu, C.-I.; Hogan, T.P.; Chung, D.-Y.; Dravid, V.P.; et al. High performance thermoelectrics from earth-abundant materials: Enhanced figure of merit in PbS by second phase nanostructures. *J. Am. Chem. Soc.* **2011**, *133*, 20476–20487. [[CrossRef](#)] [[PubMed](#)]
37. Zhao, L.-D.; He, J.; Wu, C.-I.; Hogan, T.P.; Zhou, X.; Uher, C.; Dravid, V.P.; Kanatzidis, M.G. Thermoelectrics with Earth abundant elements: High performance p-type PbS nanostructured with SrS and CaS. *J. Am. Chem. Soc.* **2012**, *134*, 7902–7912. [[CrossRef](#)]
38. Zhao, L.-D.; He, J.; Hao, S.; Wu, C.-I.; Hogan, T.P.; Wolverton, C.; Dravid, V.P.; Kanatzidis, M.G. Raising the thermoelectric performance of p-type PbS with endotaxial nanostructuring and valence-band offset engineering using CdS and ZnS. *J. Am. Chem. Soc.* **2012**, *134*, 16327–16336. [[CrossRef](#)]
39. Liu, Y.; Cadavid, D.; Ibáñez, M.; Ortega, S.; Marti-Sanchez, S.; Dobrozhan, O.; Kovalenko, M.V.; Arbiol, J.; Cabot, A. Thermoelectric properties of semiconductor-metal composites produced by particle blending. *APL Mater.* **2016**, *4*, 104813. [[CrossRef](#)]
40. Wang, Q.; Fang, Y.; Yin, H.; Li, J. Inhomogenous doping induced the imperfect self-assembly of nanocrystals for the synthesis of porous AgPb₁₀BiTe₁₂ nanosheets and their thermoelectric transport properties. *Chem. Commun.* **2014**, *51*, 1594–1596. [[CrossRef](#)]
41. Wang, Q.; Fang, Y.; Zhou, J.; Zhang, G.; Yang, L.; Huo, H. AgPb_mSbTe_{m+2} microspheres comprised of self-assembled nanoparticles driven by inhomogenous co-doping synergetic induced dipoles and their thermoelectric and electrochemical Li-storage properties. *Chem. Eng. J.* **2016**, *304*, 271–281. [[CrossRef](#)]
42. Tan, G.; Stoumpos, C.C.; Wang, S.; Bailey, T.P.; Zhao, L.-D.; Uher, C.; Kanatzidis, M.G. Subtle roles of Sb and S in regulating the thermoelectric properties of n-type PbTe to high performance. *Adv. Energy Mater.* **2017**, *7*, 1700099. [[CrossRef](#)]
43. Chen, T.; Zhang, K.; Wang, H.; Su, W.; Mehmood, F.; Wang, T.; Zhai, J.; Wang, X.; Huo, T.; Wang, C. The high thermoelectric performance of slightly Sb doped PbTe alloys. *J. Mater. Chem. C* **2020**, *8*, 1679–1685. [[CrossRef](#)]
44. Martin, J.; Nolas, G.S. Apparatus for the measurement of electrical resistivity, Seebeck coefficient, and thermal conductivity of thermoelectric materials between 300 K and 12 K. *Rev. Sci. Instrum.* **2016**, *87*, 015105. [[CrossRef](#)] [[PubMed](#)]
45. Martin, J.; Erickson, S.; Nolas, G.S.; Alboni, P.; Tritt, T.M.; Yang, J. Structural and transport properties of Ba₈Ga₁₆Si_xGe_{30-x} clathrates. *J. Appl. Phys.* **2006**, *99*, 044903. [[CrossRef](#)]
46. Van Oversteeg, C.H.M.; Oropeza, F.E.; Hofmann, J.P.; Hensen, E.J.; De Jongh, P.E.; Donega, C.D.M. Water-dispersible copper sulfide nanocrystals via ligand exchange of 1-dodecanethiol. *Chem. Mater.* **2019**, *31*, 541–552. [[CrossRef](#)]
47. Nag, A.; Kovalenko, M.V.; Lee, J.-S.; Liu, W.; Spokoyniy, B.; Talapin, D.V. Metal-free inorganic ligands for colloidal nanocrystals: S²⁻, HS⁻, Se²⁻, HSe⁻, Te²⁻, HTe⁻, TeS₃²⁻, OH⁻, and NH₂⁻ as surface ligands. *J. Am. Chem. Soc.* **2011**, *133*, 10612–10620. [[CrossRef](#)]
48. Brown, P.R.; Kim, D.; Lunt, R.R.; Zhao, N.; Bawendi, M.G.; Grossman, J.C.; Bulović, V. Energy level modification in lead sulfide quantum dot thin films through ligand exchange. *ACS Nano* **2014**, *8*, 5863–5872. [[CrossRef](#)]
49. Knight, K.S. Low temperature thermoelastic properties of galena in a simple, self-consistent, two-term Debye model. *Phys. Chem. Miner.* **2014**, *42*, 235–242. [[CrossRef](#)]
50. Tritt, T.M. *Thermal Conductivity: Theory, Properties, and Applications*; Kluwer Academic/Plenum Publishers: New York, NY, USA, 2004; ISBN 978-0-306-48327-1.
51. Goldsmid, H.; Penn, A. Boundary scattering of phonons in solid solutions. *Phys. Lett. A* **1968**, *27*, 523–524. [[CrossRef](#)]